Mixed Mg–Co spinel ferrites: Structure, morphology, magnetic and photocatalytic properties

Milena P. Dojcinovic, Zorka Z. Vasiljevic, Vera P. Pavlovic, Dario Barisic, Damir Pajic, Nenad B. Tadic, Maria Vesna Nikolic

PII: S0925-8388(20)33793-2

DOI: https://doi.org/10.1016/j.jallcom.2020.157429

Reference: JALCOM 157429

To appear in: *Journal of Alloys and Compounds*

Received Date: 4 August 2020

Revised Date: 29 September 2020

Accepted Date: 30 September 2020

Please cite this article as: M.P. Dojcinovic, Z.Z. Vasiljevic, V.P. Pavlovic, D. Barisic, D. Pajic, N.B. Tadic, M.V. Nikolic, Mixed Mg–Co spinel ferrites: Structure, morphology, magnetic and photocatalytic properties, *Journal of Alloys and Compounds* (2020), doi: https://doi.org/10.1016/j.jallcom.2020.157429.

Milena P. Dojcinovic: Synthesis, Photocatalytic characterization; Writing the original draft, Reviewing and editing, data visualisation;

Zorka Z. Vasiljevic: Synthesis, Photocatalytic characterization; Writing, reviewing and editing,

Vera P. Pavlovic: Raman spectroscopy; Data interpretation and visualisation; Writing, reviewing and editing,

Dario Barisic: Magnetic measurements, Data interpretation and visualisation,

Damir Pajic: Magnetic measurements, data interpretation and visualisation; Writing, reviewing and editing,

Nenad B. Tadic: X-ray diffraction scattering measurements,

Maria Vesna Nikolic: SEM microscopy measurements, FTIR spectroscopy measurements; UV/vis spectroscopy measurements; Writing, reviewing, editing; Data interpretation and visualisation; Conceptualization and supervision.

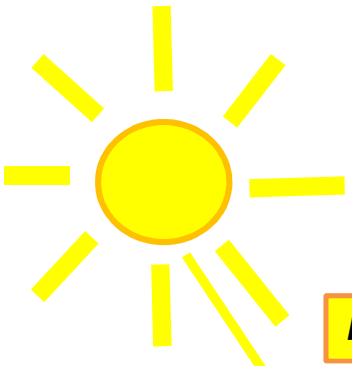

hv

e^-+h^+

$CO_2 + H_2O$

Pollutant molecule

Co↑, Mg↓

Photocatalyst surface

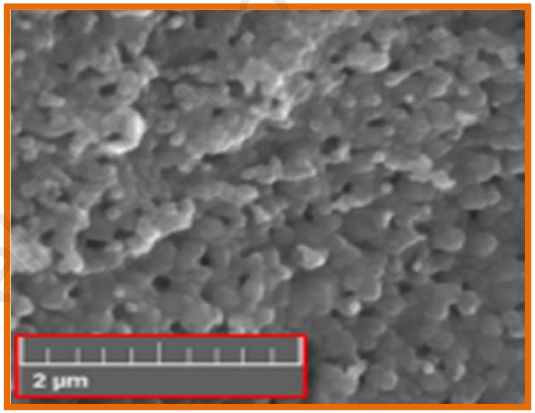

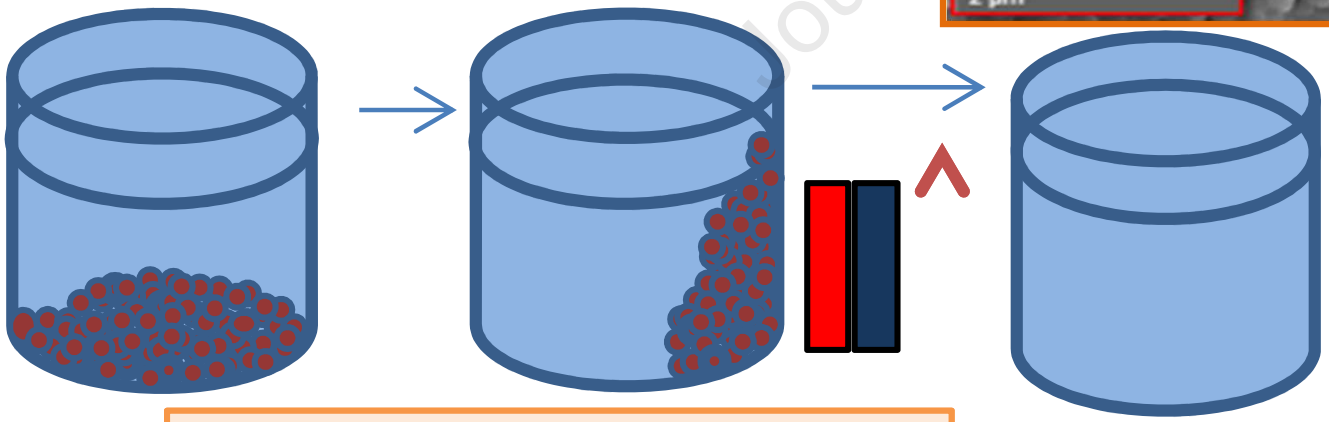

Easy magnetic photocatalyst removal

Mixed Mg-Co spinel ferrites: structure, morphology, magnetic and photocatalytic properties

Milena P. Dojcinovic[a*], Zorka Z. Vasiljevic[a], Vera P. Pavlovic[b], Dario Barisic[c], Damir Pajic[c], Nenad B. Tadic[d], Maria Vesna Nikolic[a]

[a]Institute for Multidisciplinary Research, University of Belgrade, Kneza Viseslava 1, 11030 Belgrade, Serbia

[b]University of Belgrade, Faculty of Mechanical Engineering, Kraljice Marije 16, 11120 Belgrade, Serbia

[c]Department of Physics, Faculty of Science, University of Zagreb, Bijenička 32, 10 000 Zagreb, Croatia

[d]University of Belgrade, Faculty of Physics, Studentski trg 12, 11001 Belgrade, Serbia

*corresponding author: milena.dojcinovic@imsi.rs[1]

Abstract

$Co_xMg_{1-x}Fe_2O_4$ (where *x* was 0.0, 0.1, 0.3, 0.5, 0.7, 0.9 and 1) spinel ferrites were synthesized by the sol-gel combustion method using citric acid as fuel, following the rules of propellant chemistry. Amorphous powders were then calcined at 700 °C for 3 hours. Structural analysis by X-Ray diffraction (XRD), FTIR and Raman spectroscopy confirmed the formation of a cubic spinel structure where the cation distribution and inversion degree depended on the Co^{2+} and Mg^{2+} ion content. Accordingly, the lattice parameter varied between 8.3703 Å ($MgFe_2O_4$) and 8.3919 Å ($Co_{0.9}Mg_{0.1}Fe_2O_4$) as did the crystallite size, from 34 nm ($Co_{0.1}Mg_{0.9}Fe_2O_4$) to 48 nm ($Co_{0.9}Mg_{0.1}Fe_2O_4$). Scanning electron microscopy (SEM) showed the formation of multigrain agglomerates. Determined values of the maximal and remanent magnetization, as well as coercive field, depended on the Co^{2+} and Mg^{2+} ion content and increased with substitution of diamagnetic Mg^{2+} ions with magnetic Co^{2+} ions. Most impressive is the increase of the coercive field from 74 Oe for $MgFe_2O_4$ to

[1] Email adresses: zorkav@imsi.rs (Z. Vasiljevic), vpavlovic@mas.bg.ac.rs (V. Pavlovic), dbarisic@phy.hr (D. Barisic), dpajic@phy.hr (D. Pajic), nenad.tadic@ff.bg.ac.rs (N. Tadic), mariav@rcub.bg.ac.rs (M. V. Nikolic);

1000 Oe for $CoFe_2O_4$, as well as an increase of magnetization in the field of 10 kOe from 27.4 emu g^{-1} to 75.7 emu g^{-1}. The determined optical band gaps from UV/Vis DRS measurements showed a strong dependence on cation content, morphology, and crystallite size, decreasing from 2.09 eV for $MgFe_2O_4$ to 1.42 eV for $CoFe_2O_4$. The photocatalytic efficiency of as-synthesized ferrites was investigated by monitoring photocatalytic degradation of Methylene Blue (MB) under natural sunlight, and artificial light source emitting visible light. Different conditions of MB degradation such as photocatalyst loading, molar concentration of MB, and pH values were investigated. Results have shown that under both visible light and natural sunlight, excessive amounts of cobalt retarded the photocatalytic process. $Co_{0.9}Mg_{0.1}Fe_2O_4$ showed considerable activity (74.5% after 4 hours) that is unexpected but possibly connected to structural anomalies. The best photocatalytic activity under natural sunlight was achieved by $MgFe_2O_4$ (82% after 4 hours), while the best photocatalytic activity under visible light was achieved by $Co_{0.1}Mg_{0.9}Fe_2O_4$ (79% after 4 hours).

Keywords: Spinel, Ferrites, Combustion, Structure, Photocatalysis, Magnetic properties;

1. Introduction

Current research of cubic spinel ferrites with the general formula MFe_2O_4 (where M=Co, Mg, Zn, Mn, etc.) is focused on the preparation of ferrites for a wide range of applications as magnetic materials, high frequency transformers, gas sensors, in heterogeneous catalysis and photocatalysis, for magnetic drug delivery, data storage [1, 2, 3, 4], as contrast agents in magnetic resonance imaging [5] and in the thermal activation cancer therapy (hyperthermia treatment) [6, 7, 8]. Spinel ferrites are also applied as magnetic adsorbents in wastewater treatment. Besides good adsorption capabilities, their main advantage is they can be easily located and extracted from a water medium by applying an external magnetic field [9, 10, 11].

The crystal structure of spinel ferrite compounds is cubic close packing of oxygen atoms with tetrahedral and octahedral sublattices, with M^{2+} and Fe^{3+} at two different crystallographic sites, tetrahedral and octahedral oxygen coordination (A and B sites, respectively). When the 8 A sites are occupied by M^{2+} cations and the 16 B sites are

occupied by Fe^{3+} the structure is referred to as normal spinel. If the A sites are completely occupied by Fe^{3+} ions and B sites are randomly occupied by Fe^{3+} and metal cations M^{2+} the structure is called inverse spinel. However, most spinels have a mixed (partially inverse) spinel structure when the cation distribution is mixed and both metal and Fe^{3+} cations are present on octahedral and tetrahedral sites, and an inversion parameter is used to describe the degree of inversion [12].

Magnetic materials, based on their ability to be magnetized and demagnetized, can be classified as soft and hard [13]. Magnesium ferrite is a soft magnetic n-type semiconducting material, as it loses its magnetization when excluded from the magnetic field. Spinel structures can host different types of cations of various ionic sizes without causing much structural deformation. Many cations can easily be substituted into the tetrahedral and octahedral sites in the spinel structure [14]. Changing cation distribution influences the magnetic properties of spinel ferrites [13, 15]. Cobalt ferrite is a well-known hard ferrimagnetic material with moderate magnetization and high coercivity [1,16]. Nano-sized cobalt ferrite is favorable for various applications due to its unusual properties such as magnetocrystalline high anisotropy ($1.8\text{-}3\cdot10^5$ J m^{-3} at 300 K) [17]. Cobalt ferrite has a partially inverse spinel structure with an inversion degree of about 80% [18]. Substitution of Co^{2+} for Mg^{2+} in nanocrystalline $MgFe_2O_4$ resulted in a decrease in the dielectric constant [1,19], and an increase in magnetic coercivity due to enhanced magnetocrystalline anisotropy [20]. Chirawatkul et al. [21] established that the magnetic properties of $Co_xMg_{1-x}Fe_2O_4$ nanoparticles strongly depended on the cation distribution.

Photocatalysis is a water purification method leading to pollutant mineralization and production of inorganic compounds such as CO_2 and H_2O [22, 23]. Scientific focus in this field of catalysis is on engineering efficient photocatalysts with narrower band gaps to enable better light harvesting in the visible light domain, especially when using sunlight as the energy source because its spectral maximum lies in the visible region. Spinel ferrites have a relatively narrow band gap (ca. 2.0 eV) so they can absorb both visible and ultraviolet radiation and are suitable materials for investigating the possible application as photocatalysts [4, 24, 25]. The added advantage of the use of spinel ferrites as photocatalysts is their magnetic nature, enabling easy separation and removal of the catalyst from the mixture in the reactor [11, 26]. Photocatalysis is proved to be dependent

upon the nature of photocatalyst and pollutant, but is also greatly influenced by particle and grain size, agglomeration degree, the geometry of the reactor, ambient conditions, etc [4, 20, 23, 26, 28].

In the present work we prepared and characterized spinel ferrites with the general formula $Co_xMg_{1-x}Fe_2O_4$ by substituting Mg^{2+} ions with Co^{2+} ($0 \leq x \leq 1$) using a simple sol-gel method. The aim was to analyze how the different cation content and distribution resulting from the preparation procedure (citrate combustion followed by calcination) influence the microstructure, magnetic and photocatalytic properties in the visible light region in both natural sunlight and using an artificial light source in order to achieve an optimal composition and morphology for efficient photocatalytic activity.

2. Experimental

Spinel magnesium cobalt ferrites were synthesized by a sol-gel combustion method using citric acid (Sigma Aldrich, ACS) as a reducing agent and nitrate ions as oxidizers. The chemicals used were $Mg(NO_3)_2 \cdot 6H_2O$ (Sigma Aldrich, puriss, p. a.), $Co(NO_3)_2 \cdot 6H_2O$ (Sigma Aldrich, puriss, p. a.), and $Fe(NO_3)_3 \cdot 9H_2O$ (Sigma Aldrich, puriss, p. a.). All chemicals used in synthesis were used without further purification. The obtained brown/black powders were calcined for 3 hours at 700 ° C with 1 h heating time.

Diffraction data were acquired over the scattering angle from 10 to 90° with a step of 0.05 s with an acquisition rate of 1 ° min^{-1} using a Rigaku Ultima IV diffractometer in Bragg-Bretano geometry. Irradiation used was Ni-filtered Cu K_α radiation with the wavelength of 1.54178 Å. Structural refinements were performed using the Rietveld method and the GSAS II package [29].

Raman spectra were recorded using a 532 nm laser on an XploRA (Horiba Jobin Yvon) spectrometer at room temperature in the Raman shift region of 100-1000 cm^{-1}. The power at sample was 2.5 mW.

Scanning electron microscopy (SEM) was used for morphological and microstructure analysis on a TESCAN Electron Microscope VEGA TS 5130 MM. Fourier transform infrared (FTIR) spectra were recorded on a FT-IR Nicolet 6700 ATR device in the range 400-2000 cm^{-1}, with a resolution of 4 cm^{-1}. UV/Vis diffuse reflectance spectra of the

obtained powders were measured on a Shimadzu UV-2600 with an ISR2600 Plus integrating sphere attachment in the measuring range 200-1200 nm.

Magnetic hysteresis curves were measured using the Vibrating-Sample Magnetometer (VSM) model PAR/EG&G 4500. Samples in powder form were pressed in a gelatin ampoule which was tightly fastened to the sample rod, in order to avoid the rotation of the powder. Measurements were performed at room temperature, with maximum magnetic field of 10 000 Oe (1 T). Constant magnetic field sweep rate of 1000 Oe/min was used and for each measured curve 1000 data points were collected. The driving frequency of the sample and integration time were 82 Hz and 100 ms, respectively.

Photocatalytic degradation of aqueous solutions of Methylene Blue (Methylene Blue, MB, Sigma-Aldrich) was investigated under visible light irradiation using a halogen lamp (70 mW cm^{-2}). 10 mg of the prepared photocatalysts were dispersed in 50 ml of MB aqueous solution with a concentration of 10 mg L^{-1} in a reaction cell. Photocatalytic degradation of MB was also carried out under direct natural sunlight in July and August 2019 between 11 am to 3 pm when the temperature was between 30 and 33 °C and light intensity was 800-1100 W/m^2, measured with Voltcraft solar radiation measuring instrument PL-110SM. To distinguish the degradation effect from adsorption, prior to illumination the suspension was left in the dark for 60 minutes for the adsorption/desorption equilibrium to occur. At given time intervals, 3 mL aliquots were sampled and centrifuged (6000 rpm, 5 min) to remove photocatalyst powders. Changes in concentrations of the MB solution were recorded at the wavelength of 663 nm by using a Shimadzu UV-2600 spectrophotometer in the interval of 200-800 nm. We further studied photocatalytic degradation of as-synthesized spinel ferrites for different pH values (2-10) of the pollutant (MB) solution, and also the influence of different concentrations of pollutant and doses of photocatalyst on photocatalytic degradation of MB.

3. Results and discussion

3.1 XRD analysis

Rietveld refinement of the XRD diffractograms measured for $Co_xMg_{1-x}Fe_2O_4$ spinel ferrites ($0 \leq x \leq 1$), shown in Figure 1, enabled the determination of unit cell parameters,

atomic positions, and inversion degree (the degree of inversion is defined as the percentage of Fe^{3+} ions occupying the tetrahedral (A) positions in the cubic lattice [30]). Traces of hematite (α-Fe_2O_3) were only noted in $MgFe_2O_4$, and this has previously been noted for this ferrite [30]. The crystallite size was determined using the Sherrer equation. A summary of the obtained parameters is given in Table 1, while detailed parameters are given in Table 1s (Supplemental data). The crystallite size increased with increase in cobalt mole percentage from 34 nm ($Co_{0.1}Mg_{0.9}Fe_2O_4$) to 48 nm ($Co_{0.9}Mg_{0.1}Fe_2O_4$), which is expected due to higher ionic radii and has been noted before for Co^{2+} ion doping [31]. The determined inversion degree varied between 0.56 and 0.91 depending on the Co^{2+} ion and Mg^{2+} content and their distribution on tetrahedral and octahedral sites, together with Fe^{3+} ions. The lattice parameter also varied according to the content and distribution of ions and was between 8.3703 Å ($MgFe_2O_4$) and 8.3919 Å ($Co_{0.9}Mg_{0.1}Fe_2O_4$).

In synthesized $MgFe_2O_4$ powder, Mg^{2+} and Fe^{3+} ions are located on both octahedral (B) and tetrahedral (A) sites, though more Mg^{2+} ions are on B sites. According to Chirawatkul et al. [21] no site preference can be assumed for Mg^{2+} as a non-magnetic cation, so it is likely for $MgFe_2O_4$ to be a partially inverse spinel, though according to Sun et al. [32] Mg^{2+} has a "burning" preference for B sites. The percentage of total Mg^{2+} occupying the tetrahedral site has varied from 10-29%, though Henderson et al. determined 50% [12] and in literature the inversion degree for $MgFe_2O_4$ varies from 0.1 to 1 [21]. In our case, the inversion degree was 0.79, thus with 21% Mg^{2+} cations on A sites. The determined lattice constant value falls within the range of previously determined values for magnesium ferrite [33].

For synthesized $CoFe_2O_4$ powder the inversion degree was the same as for $MgFe_2O_4$ (0.79) only in this case it is Co^{2+} ions (0.21 on tetrahedral sites). Chirawatkul et al. [21] concluded in accordance with the crystal field theory that Co^{2+} ions would be more stable on octahedral sites, as the most stable configuration of the 7 electrons in the 3*d* orbital would be $t_{2g}^5\, e_g^2$. Venturini et al. [34] achieved the switching of the spinel inversion degree by excess cations of either iron or cobalt. They also concluded that the synthesis parameters of the sol gel combustion process have a strong and significant influence on

cation positioning, as their determined degree of inversion for the nominal $CoFe_2O_4$ composition was 0.25.

When Co^{2+} ions are introduced into $MgFe_2O_4$, they compete with Mg^{2+} for both A and B sites [1]. Mg^{2+} substituted $CoFe_2O_4$ or Co^{2+} substituted $MgFe_2O_4$ have been investigated before. Sundararajan et al. [25] noted a diffraction peak shift to lower diffraction angles with Mg^{2+} addition up to x = 0.5. According to Chirawatkul et al. [21] the value of the lattice constant (a) increased with an increase in Co^{2+} content in the Mg-Co ferrite mixtures obtained by the sol-gel combustion process, though Druc et al. [1] noted the opposite for Mg-Co ferrite mixtures obtained also by sol-gel combustion and subsequent calcination at 900 ^{o}C. In our samples, when the amount of cobalt is low (0.1 and 0.3) cobalt cations occupy only octahedral (B) sites, the inversion degree is high (0.91 and 0.88, respectively). We can also observe an increase in the lattice constant with the addition of Co^{2+} (x = 0.1 and 0.3), as shown in Table 1, and a slight (311) peak shift towards lower values.

When the amount of cobalt and magnesium is the same (0.5), the inversion degree decreases to 0.56, most cobalt ions are on A sites (0.44) and most magnesium ions are on B sites (0.49), the lattice constant decreases and the (311) peak has shifted to slightly higher values. When the amount of cobalt is higher (0.7 and 0.9), magnesium ions are located only on B sites, cobalt ions are on both sites, while the inversion degree varies and is 0.75 for x=0.7 and 0.6 for x=0.9. The lattice constant increases with an increase in cobalt content, while the (311) peak shifts to lower values. Overall the lattice constant value is the highest for x=0.9 and the (311) peak is at the lowest value of 2θ, showing that the cation distribution besides the cation content influences these parameters.

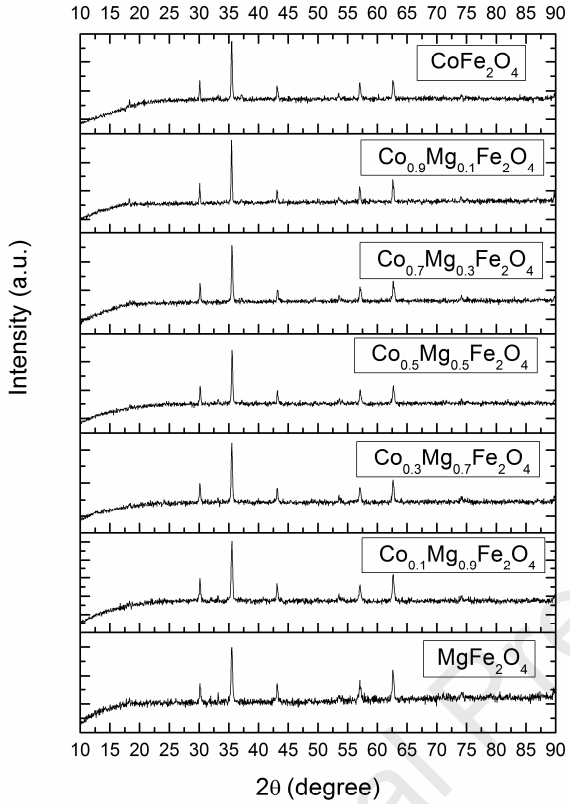

Figure 1. XRD diffractograms of $Co_xMg_{1-x}Fe_2O_4$ spinel ferrite powders ($0 \leq x \leq 1$)

Table 1. Lattice parameter, inversion degree, crystallite size and direct band gap determined for $Co_xMg_{1-x}Fe_2O_4$ spinel ferrites ($0 \leq x \leq 1$)

Sample	Lattice parameter *a* (Å)	Inversion degree	Crystallite size (nm)	Direct band gap (eV)
$MgFe_2O_4$	8.3703(8)	0.79	36	2.09
$Co_{0.1}Mg_{0.9}Fe_2O_4$	8.3829(6)	0.91	34	1.96
$Co_{0.3}Mg_{0.7}Fe_2O_4$	8.3847(5)	0.88	38	1.80
$Co_{0.5}Mg_{0.5}Fe_2O_4$	8.3750(5)	0.56	42	1.58
$Co_{0.7}Mg_{0.3}Fe_2O_4$	8.3779(5)	0.75	41	1.44

$Co_{0.9}Mg_{0.1}Fe_2O_4$	8.3919(4)	0.60	48	1.39
$CoFe_2O_4$	8.3878(5)	0.79	41	1.42

The crystallite size varied with the content of cobalt and magnesium ions, with the highest value obtained for $Co_{0.9}Mg_{0.1}Fe_2O_4$ (48 nm) and the lowest for $Co_{0.1}Mg_{0.9}Fe_2O_4$ (34 nm).

3.2. Raman spectra analysis

Analyses of Raman spectra of $Co_xMg_{1-x}Fe_2O_4$ spinel ferrite powders ($0 \leq x \leq 1$) (Figure 2) show the presence of modes characteristic for cubic spinel ferrites (the five Raman active modes $A_{1g} + E_g + 3T_{2g}$ according to factor group analysis [30, 35]) with a partially or completely inverse spinel structure [36, 37, 38, 39]. The peak intensities depended strongly on the distribution of Mg^{2+}, Co^{2+} and Fe^{3+} ions. In the Raman spectra of spinel ferrites, the A_{1g} peak originates from symmetric breathing modes of the AO_4 unit, also known as the tetrahedral breath modes, wherein our case A could be M (Mg^{2+} or Co^{2+}) or Fe^{3+} ions [40, 41, 42]. The T_{2g} (2) and T_{2g} (3) modes originate from ion vibrations of octahedra, where the T_{2g} (2) mode originates from asymmetric stretching vibrations of (Fe/M)–O bonds, while T_{2g} (3) originates from asymmetric bending vibrations of (Fe/M)–O bonds [43]. The E_g mode corresponds to symmetric bending vibrations of (Fe/M)–O bonds, while the T_{2g} (1) is related to translational AO_4 tetrahedral vibrations [40, 41, 44]. Additional modes, besides the five Raman active modes that follow from the group symmetry theory, are often present in spinel ferrites in the form of asymmetry in Raman peaks. This can be seen in the Raman spectra of our $Co_xMg_{1-x}Fe_2O_4$ spinel ferrites (Figure 2). The basic reason for this is the redistribution of Fe^{3+} and bivalent metal ions (Co^{2+} and Mg^{2+}) on tetrahedral and octahedral sites. Asymmetry of the A_{1g} peak, expressed as a shoulder effect, is marked as A_{1g} (2) in Figure 2.

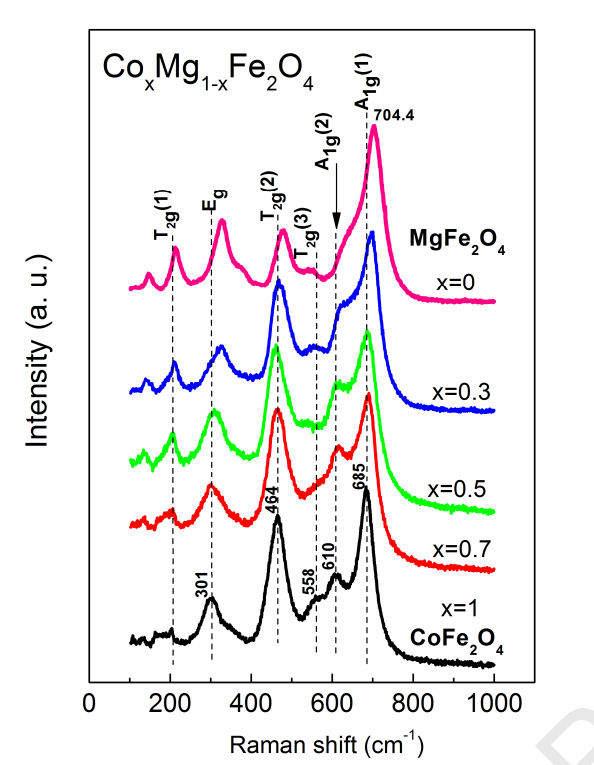

Figure 2. Raman spectra of $Co_xMg_{1-x}Fe_2O_4$ spinel ferrite powders (x =0, 0.3, 0.5, 0.7 and 1)

There are different views in literature on the origin of A_{1g} (1) and A_{1g} (2) peaks, especially concerning $MgFe_2O_4$. One view is that the occurrence of the A_{1g} (2) shoulder is due to redistribution of cations on tetrahedral sites, i. e. due to the presence of an inverse or mixed spinel structure. Some authors [45, 46] attribute the Mg–O bond to the A_{1g} (1) peak, while others attribute it to the A_{1g} (2) peak [47]. The same can be said of partially inverse and mixed spinel $CoFe_2O_4$ where there are also different interpretations of the origin of A_{1g} (1) and A_{1g} (2) modes (Fe–O or Co–O bonds). The prevailing opinion is that the A_{1g} (2) mode at ~ 610 - 640 cm^{-1} originates from vibrations of Co–O bonds inside CoO_4 tetrahedron, while the mode at higher Raman shift value originated from Fe–O bonds inside FeO_4 tetrahedron [48, 49] and our results confirm this assumption.

Analysis of the Raman spectra of our $Co_xMg_{1-x}Fe_2O_4$ spinel ferrites (Figure 2) shows that there is a noticeable red shift of all peaks except T_{2g} (3) with an increase in Co^{2+} content and decrease in Mg^{2+} content. Similar behavior was noted by Mund et al. [50]. This red shift can be explained by the lengthening of the M^{2+}–O ionic bond and increase of the

reduced mass for that bond, due to the larger radius and mass of the Co^{2+} ion compared to Mg^{2+} (Table 1s). The opposite behavior of the T_{2g} (3) mode attributed to asymmetric bending vibrations on octahedral sites has also been noted when nickel ferrite was doped with magnesium ions [40]. Analysis of the measured X-ray diffractogram of $CoFe_2O_4$ has shown that a partially inverse spinel structure was obtained (Table 1), with Co^{2+} ions present on both octahedral and tetrahedral sites. Taking this into account and the Raman spectra obtained for $Co_xMg_{1-x}Fe_2O_4$ samples we can conclude that the A_{1g} (2) peak noted at about 610 cm^{-1} originates from the presence of Co^{2+} ions on octahedral sites. In $CoFe_2O_4$ the T_{2g} (2) peak (related to the ion vibrations of octahedra) is significantly more expressed than the A_{1g} (2) peak, in the sample. The contribution of the presence of Fe^{3+} ions on octahedral sites should also be taken into account in the case of T_{2g} (2). Rietveld analysis of X-ray diffraction spectra of $Co_xMg_{1-x}Fe_2O_4$ showed that reduction of *x* from 1 to 0.5 (increase in Mg^{2+} content) is accompanied by the redistribution of cobalt between tetrahedral (A) and octahedral (B) sites. When *x* changes from 1 to 0.7 cobalt (Co^{2+}) ions move from octahedral to tetrahedral sites, as magnesium ions prefer octahedral sites for low concentrations of Mg^{2+}. The preference of Mg^{2+} ions for octahedral sites, compared to Co^{2+} and Fe^{3+} ions, is mentioned by Ehi-Erimosele et al. [51]. In our Raman spectra, this is marked by the relative increase of the A_{1g} (2) mode (A sites for cobalt ions) and decrease of the intensity of the T_{2g} (3) mode (dominant contribution of asymmetric bending vibrations of Co–O bonds in the octahedra), with the decrease of *x* value to 0.7. At $x = 0.5$ we can note the appearance of the shifted T_{2g} (3) peak due to the increased presence of asymmetric bending vibrations of Mg–O bonds in the octahedra. The A_{1g} (1) peak gradually decreases due to the transition of Fe^{3+} ions from A to B sites, due to the mentioned redistribution of Co^{2+} ions. The T_{2g} (2) peak remains quite intensive, as it originates from the contribution of all ion types to asymmetric stretching vibrations in octahedral sites. Further decrease of *x* below 0.5 leads to a reduction of the concentration of cobalt ions on tetrahedral sites, with a simultaneous increase of iron and magnesium ions on these sites. Due to this, the A_{1g} changes form and position, slowly approaching the characteristic look for $MgFe_2O_4$. In the Raman spectrum of $MgFe_2O_4$, compared to $C_{0.3}Mg_{0.7}Fe_2O_4$, the significant decrease in the T_{2g} (2) intensity with the respect of A_{1g} mode intensity is noticed. It is in accordance with the general observation that in $MgFe_2O_4$ spectra the T_{2g} (2) mode is less expressed

compared to the A_{1g} peak than in $NiFe_2O_4$ or $CoFe_2O_4$, at least for spectra of nanoparticle systems obtained using the 532 nm laser excitation wavelength, as noted in [40, 51], though Raman spectra of $MgFe_2O_4$ ferrites depend on the synthesis method, particle size, degree of inversion of the spinel structure and the laser excitation wavelength.

3.3. SEM analysis

SEM images of the $Co_xMg_{1-x}Fe_2O_4$ spinel ferrite powders ($0 \le x \le 1$) are shown in Figure 3.

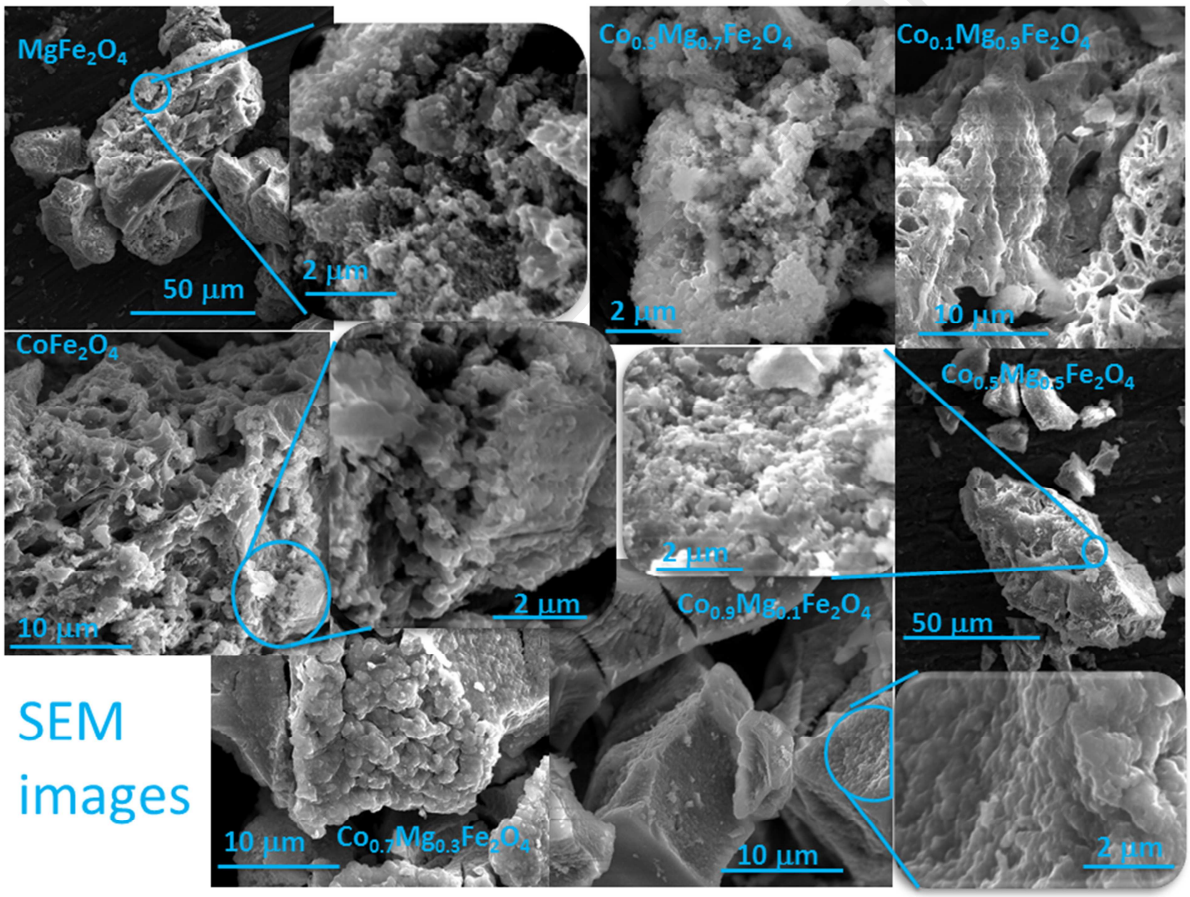

Figure 3. SEM images of $Co_xMg_{1-x}Fe_2O_4$ spinel ferrite powders ($0 \le x \le 1$)

The presence of agglomerates is noticeable in all $Co_xMg_{1-x}Fe_2O_4$ spinel ferrite ($0 \le x \le 1$) powders. Multigrain agglomerates have been observed for magnesium cobalt ferrite mixtures before [51]. This has been attributed to magnetic dipole interactions between ferrite particles [20] or interfacial surface tension phenomenon [25]. As the Co^{2+} content increases, the agglomerates visible by scanning electron microscopy are composed of

compacted particles that are almost melted together, as can be noted especially for $Co_{0.7}Mg_{0.3}Fe_2O_4$ and $Co_{0.9}Mg_{0.1}Fe_2O_4$ samples. Assi et al. [52] noted densely connected grains in $CoFe_2O_4$ due to interactions between magnetic nanoparticles and also interfacial surface tension. They also noted that samples with more magnesium were less agglomerated which can be due to the replacement of magnetic cobalt ions with diamagnetic magnesium ions.

3.4 FTIR spectra analysis

FTIR spectra measured for the synthesized $Co_xMg_{1-x}Fe_2O_4$ spinel ferrite powders ($0 \leq x \leq 1$) are shown in Figure 4. No organic phases nor nitrate groups were noted. Only peaks originating from the cubic spinel structure can be noted in the range 400-830 cm^{-1}. Two peaks were noted for all mixtures. For $CoFe_2O_4$ they were at $\nu_1 = 550\ cm^{-1}$ and $\nu_2 = 418\ cm^{-1}$ thus confirming the formation of M–O (M=Co, Fe) bonds at tetrahedral (A) and octahedral (B) sites, respectively in accordance with literature data [1, 20]. The shift of the ν_1 band with the change of cobalt content is caused by the substitution of iron and magnesium ions with cobalt ions on the tetrahedral sites. The heavier Co^{2+} ions substitute the proportional amount of Mg^{2+} ions resulting in an increase in the wavenumber of peaks, as noted before [1, 50].

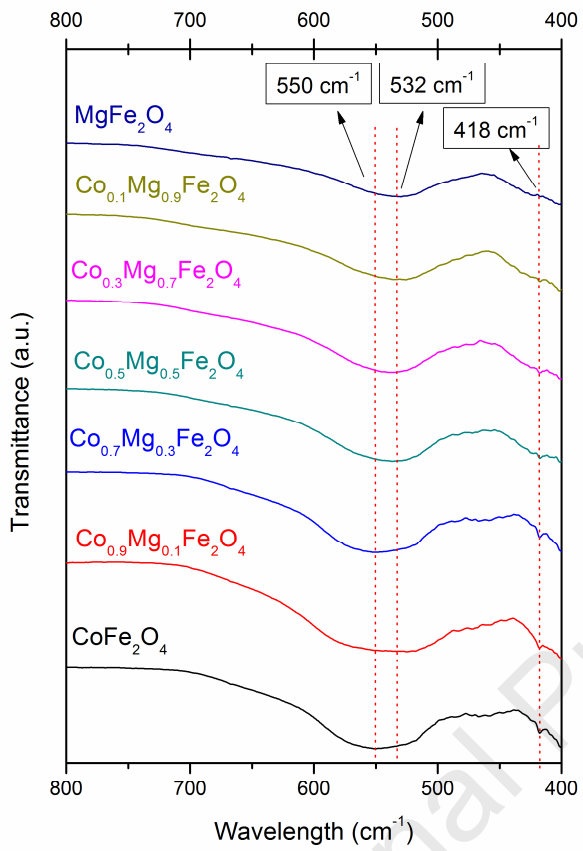

Figure 4. FTIR spectra of $Co_xMg_{1-x}Fe_2O_4$ spinel ferrite powders ($0 \leq x \leq 1$)

3.5 UV/Vis spectra analysis

The Tauc model for a direct system [53] was used to determine the optical band gaps of $Co_xMg_{1-x}Fe_2O_4$ spinel ferrite powders ($0 \leq x \leq 1$): $\alpha \times h\nu = A\,(h\nu - E_g)^m$, where $h\nu$ is the absorbed photon energy, A denotes a constant linked with the density of electronic states above and below the band gap, E_g is the determined band gap, while m takes different values depending on the type of transition from the valence to the conduction band. In the case of a direct transition $m = ½$, which is the case for magnesium or cobalt cubic spinel ferrites [54]. The equivalent absorption coefficient (α) was calculated from the measured diffuse reflectance spectra using the Kubelka-Munk function. The optical band gap E_g was determined as shown in Figure 5 and the obtained values are given in Table 1. It

is noticeable that the band gap value decreases with an increase in cobalt content and a reduction in magnesium content. This has been noted before by Sundararajan et al. [25]. Low values of the optical band gap (between 1.4 and 2.0 eV) have previously been determined for nanostructured $CoFe_2O_4$ [54]. The band gap of pure magnesium ferrite is slightly lower (2.09 eV) than some literature values (2.18 eV [3]). Interfacial defects as a result of the formation of additional sub-band energy levels in agglomerated spinel nanoparticles can be the cause of overall lower optical band gap values determined in nanostructured spinel ferrites compared to the bulk samples [25].

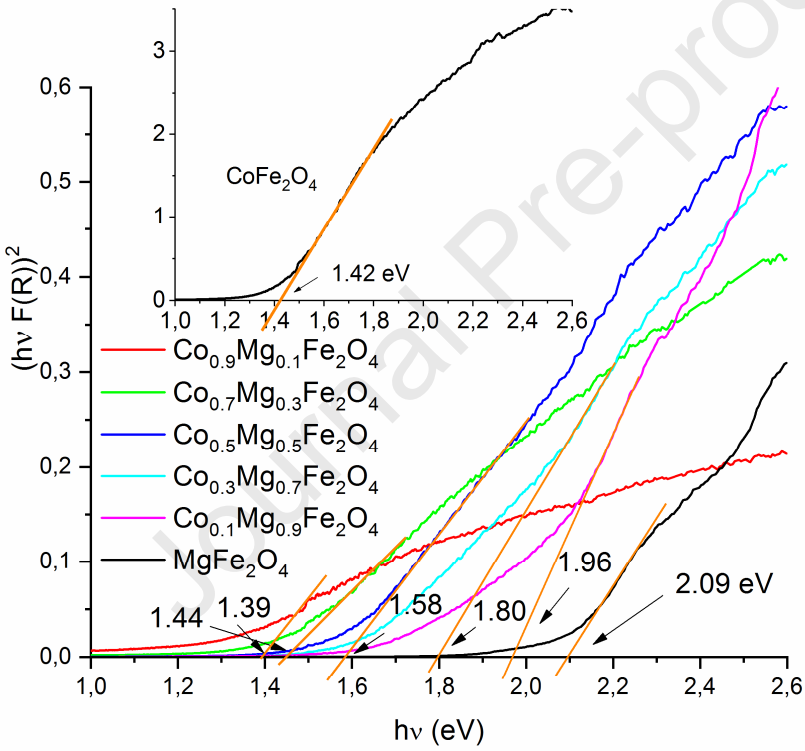

Figure 5. Estimation of optical band gap values for direct transition from Tauc plots of diffuse reflectance spectra of $Co_xMg_{1-x}Fe_2O_4$ spinel ferrite powders ($0 \leq x \leq 1$)

It is interesting to note that the lowest optical band gap value was determined for $Co_{0.9}Mg_{0.1}Fe_2O_4$ (1.39 eV), with slightly higher values for $CoFe_2O_4$ (1.42 eV) and $Co_{0.7}Mg_{0.3}Fe_2O_4$ (1.44 eV). This could be linked with the sample morphology and crystallite size as a result of differences in the synthesis method as previously noted for $CoFe_2O_4$ [16,

55], besides the cation content (magnesium to cobalt molar ratio) and distribution. Sundararajan et al. [25] calculated the band edge positions for $Co_{1-x}Mg_xFe_2O_4$ ($0 \leq x \leq 0.5$) spinel nanoparticles, and showed that addition of x=0.1 of magnesium ($Co_{0.9}Mg_{0.1}Fe_2O_4$) shifted the valence band (VB) potential edge to be less positive and the conduction band (CB) potential edge to be more negative compared to pure $CoFe_2O_4$. Further increase of magnesium content gradually increases the VB edge to more positive values and the CB edge moves from less negative to positive values.

3.6 Magnetic properties

Measured magnetic hysteresis loops at room temperature are shown in Figure 6, where monotonous development of the loops with Mg-Co substitution can be observed. The increase of magnetization, as well as broadness of the hysteresis loops, occurs with the substitution of diamagnetic Mg^{2+} ions with cobalt Co^{2+} ions.

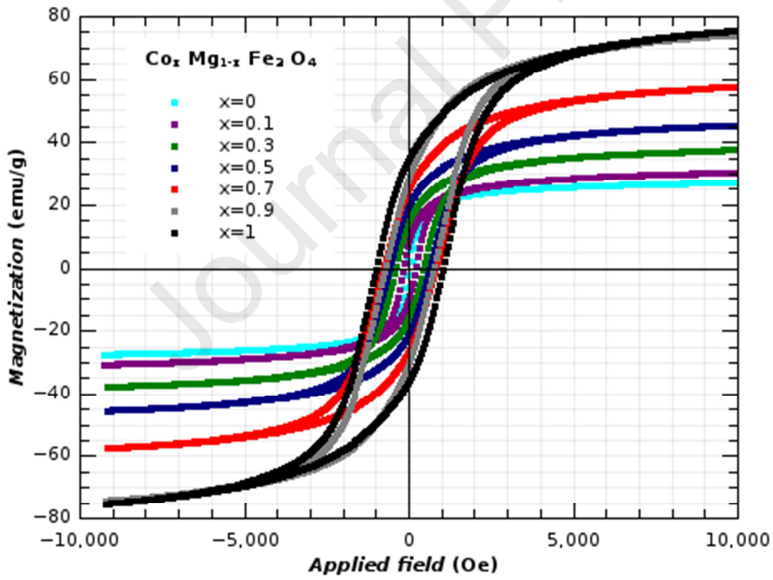

Figure 6. Magnetic hysteresis curves at room temperature for different concentrations of Co (Mg) in $Co_xMg_{1-x}Fe_2O_4$

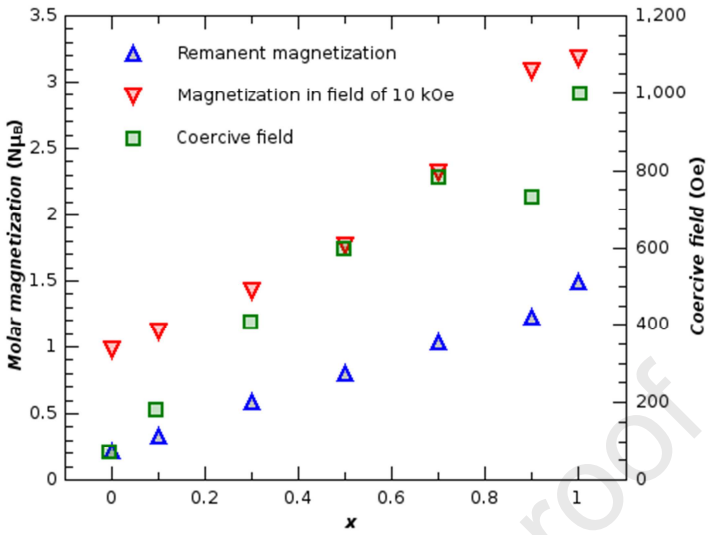

Figure 7. Hysteresis curve parameters for different concentrations of Co (Mg) in $Co_xMg_{1-x}Fe_2O_4$

Table 2. Magnetization M in the field of 10 kOe (in both units Bohr's magneton per formula unit and emu/g), remanent magnetization M_R and coercive field H_C for $Co_xMg_{1-x}Fe_2O_4$ spinel ferrites ($0 \le x \le 1$)

x	M in 10 kOe (μ_B per f.u.)	M in 10 kOe (emu/g)	M_R (μ_B per f.u.)	H_C (Oe)
0.0	0.981	27.38	0.208	74.0
0.1	1.119	30.72	0.328	182.5
0.3	1.422	37.75	0.581	407.5
0.5	1.770	45.50	0.802	600.0
0.7	2.316	57.69	1.035	785.0
0.9	3.082	74.47	1.222	732.5
1.0	3.179	75.68	1.488	1000.0

Parameters extracted from the hysteresis loops are shown graphically in Figure 7. and listed in Table 2. Obtained results exhibit almost linear dependence of remanent

magnetization, coercive field and magnetization in the field of 10 kOe on the concentration of *x*. The slightly larger deviation for the sample with *x*=0.9 is in agreement with other anomalies observed for this concentration (microstructure, crystallite size, optical band gap). Magnetic parameters for pure Co and Mg ferrites are in good agreement with existing data, for example, saturation magnetic moments listed in [56] are 1.1 μ_B for $MgFe_2O_4$ and 3.7 μ_B for $CoFe_2O_4$ formula units. Accordingly, magnetic parameters obtained for $CoFe_2O_4$ in this work lie in the range of values obtained for $CoFe_2O_4$ nanoparticles synthesized using conventional and microwave heating [16, 55]. This increase of the magnetic moment is the consequence of the additional unpaired electrons sitting on Co^{2+} ions that are introduced into the ferrite lattice instead of the Mg^{2+} ions. The coercive field increases with cobalt content, which can be understood as a consequence of stronger spin-orbit coupling usual for cobalt ions leading to larger anisotropy and therefore to the harder reversal of their magnetic moments, causing stronger pinning of the domain walls, i.e. more difficult change of magnetic domain structure. The same reasoning applies to the remanence of the studied series. Observed large magnetization of the material would make it suitable for the removal from the solution using moderate magnetic fields produced by widely accessible permanent magnets like Nd-Fe-B. This removal would be more efficient with increased content of cobalt in the ferrite. Investigations of the separation efficiency of magnetic spinel ferrites have shown that they are highly stable and reusable [26, 31, 55],

3.7 Photocatalytic degradation of methylene blue dye

3.7.1 Effect of composition

Photocatalytic degradation by powders with different mole percentages of cobalt in $Co_xMg_{1-x}Fe_2O_4$ under the halogen lamp irradiation is shown in Figure 8. $MgFe_2O_4$ has a better activity (63.4%) than $CoFe_2O_4$ (47%), which can be explained with the already established quality of magnesium ferrite as a photocatalyst [2], and a lesser degree of agglomeration of $MgFe_2O_4$ compared to other synthesized powders. Introducing cobalt ions into the crystal structure in small cobalt to magnesium molar ratios enhances the photocatalytic degradation of magnesium ferrite (*x*=0.1 (78.8%), *x*=0.3 (74.8%)). The best photocatalytic degradation efficiency under visible light was shown by $Co_{0.1}Mg_{0.9}Fe_2O_4$. After 240 min, the degradation of MB dye was almost 80% for $Co_{0.1}Mg_{0.9}Fe_2O_4$, respectively.

Pure $CoFe_2O_4$ degraded only 47% of the dye during 240 minutes. Similar results were obtained by Gan et al. [57] In their investigation, 50 mg of $CoFe_2O_4$ degraded 34% of 200 ml methylene blue dye concentration of 10 mg L^{-1} .

$Co_{0.9}Mg_{0.1}Fe_2O_4$ showed considerable activity (74.5%) which is unexpected but might be connected to the structural anomalies which appeared in this particular material and which are evident in magnetic and structural investigations.

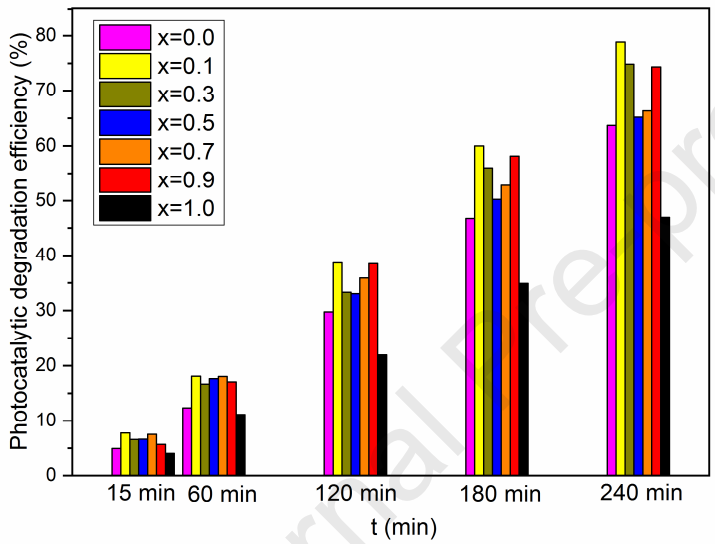

Figure 8. Photocatalytic degradation efficiency of MB (10 mg L^{-1}) in aqueous solution using spinel $Co_xMg_{1-x}Fe_2O_4$ (x=0.0, 0.1, 0.3, 0.5, 0.7, 0.9, 1.0) under visible light irradiation

The results obtained for photocatalytic activity of $Co_xMg_{1-x}Fe_2O_4$ spinel ferrites under natural sunlight are shown in figure 9.

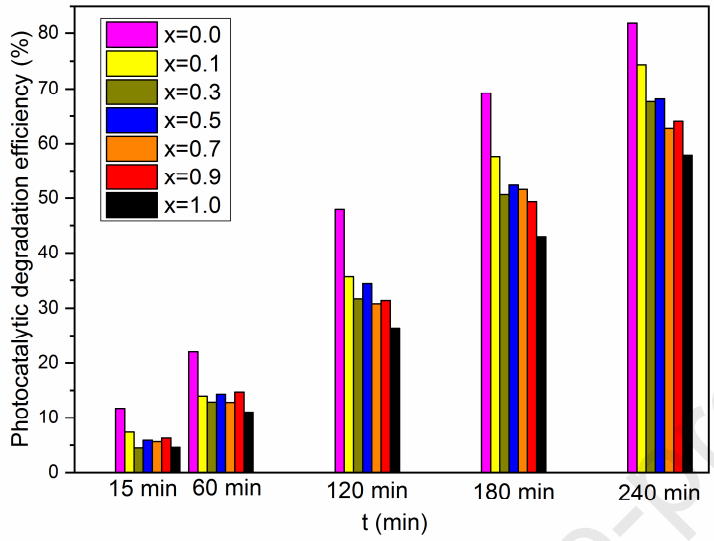

Figure 9. Photocatalytic degradation efficiency of MB aqueous solution (10 mg L^{-1}) using spinel $Co_xMg_{1-x}Fe_2O_4$ (x=0.0, 0.1, 0.3, 0.5, 0.7, 0.9, 1.0) under natural sunlight irradiation

The best photocatalytic activity under natural sunlight (Fig 9.) was shown by $MgFe_2O_4$ (82% after 240 minutes). Excessive amounts of cobalt in the spinel structure slowed down the photocatalytic process, which is consistent with previously reported results. [20, 58]. This may be due to the change of morphology of the calcined powders, which formed harder and more compacted agglomerates with the increase of the cobalt mole percentage in the composition of the spinel structure. Reaction rate constants along with related errors extracted from the kinetic curves calculated with the first-order kinetics model are presented in Table 3. Godlyn Abraham et al. [20] and Assi et al. [52] also determined that Co doping of $MgFe_2O_4$ enhances the photocatalytic activity and but excessive amounts slow the process. The same thing was observed by Lynda et al. [59] in the case of doping $MgFe_2O_4$ with zinc cations.

Table 3. Reaction rate constants extracted from the kinetic curves calculated with the first-order kinetics model

X	Natural sunlight	Visible light

	k ($\cdot 10^{-3}$ min^{-1})	k ($\cdot 10^{-3}$ min^{-1})
0	6.6±0.4	3.7±0.3
0.1	5.0±0.4	5.6±0.4
0.3	4.2±0.3	5.0±0.4
0.5	4.3±0.3	4.0±0.2
0.7	3.9±0.2	4.3±0.2
0.9	3.9±0.2	5.1±0.3
1.0	3.2±0.2	2.4±0.1

3.7.2 Effect of catalyst loading

Optimum catalyst loading is crucial in optimizing a photocatalytic process due to the economic aspect of minimizing waste and achieving maximal efficiency. In order to understand the correlation between catalyst loading and photodegradation efficiency, in this work we investigated the degradation of 10 mg L^{-1} MB aqueous solution using spinel $Co_{0.1}Mg_{0.9}Fe_2O_4$ under visible light irradiation with different catalyst loading – 10, 30 and 50 mg per 50 ml of dye solution (Figure 10). The optimum weight of catalyst loading was 30 mg per 50 ml of dye solution. Further increase in catalyst loading resulted in a decrease in the reaction rate as shown in Figure 10. Similar results were obtained by Padmapriya et al. where photocatalytic degradation efficiency of mixed Ni-Zn spinels also increased with catalyst dosage up to 30 mg per 100 mL^{-1}, after which efficiency decreased [60]. This is caused by active sites on the catalyst surface and penetration of light into the suspension. Active sites on the surface of the photocatalyst would increase with increasing catalyst loading. However, above optimum catalyst loading, light penetration in the solution decreases due to the screening effect of excess catalyst particles [61].

Kinetic curves drawn with the first-order kinetics model are shown in Figure 10. It can be concluded that moderate loading of the photocatalysts is optimal for this $Co_xMg_{1-x}Fe_2O_4$ spinel ferrites-methylene blue dye system.

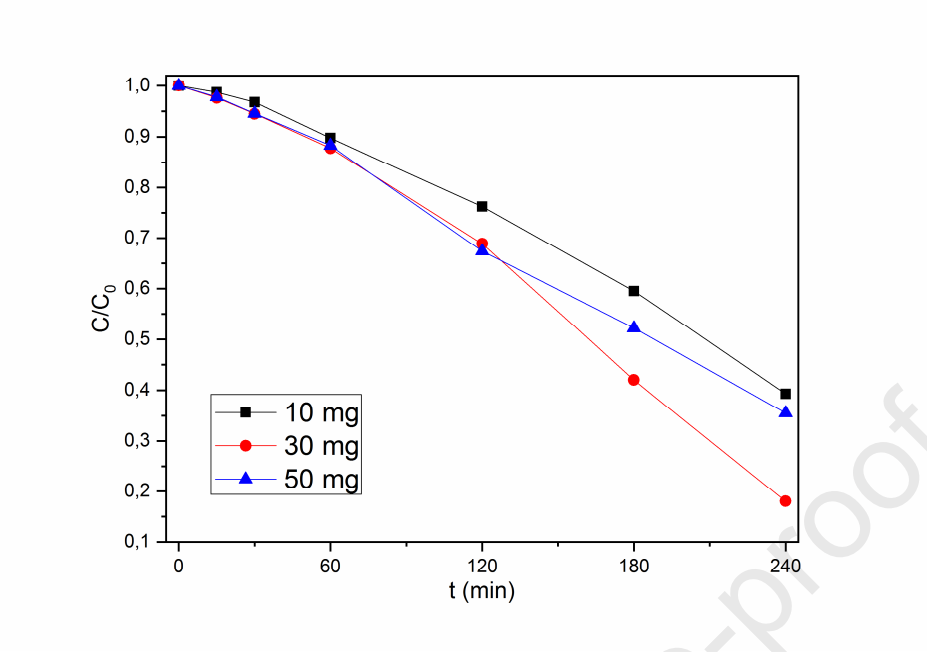

Figure 10. C/C_0 *vs.* time plot for different catalyst loading (initial MB concentration was 10 mg L^{-1}, visible light irradiation) analyzed for $Co_{0.1}Mg_{0.9}Fe_2O_4$

3.7.3 Effect of dye concentration

In order to study the effect of initial dye concentration on the photocatalytic activity for $Co_{0.1}Mg_{0.9}Fe_2O_4$ catalyst (50 mg) a set of experiments was carried out in order to find the optimal dye concentration by increasing the dye concentration from 5 to 20 mg L^{-1} (Figure 11) under natural sunlight.

Reaction rate constants were calculated from the slopes of the kinetic curves and they are shown as an inset in Figure 11. A faster reaction is attributed to the lower concentrations (5 mg L^{-1} and 10 mg L^{-1}) which means that they are desirable for a faster and more efficient reaction. This result is also predicted and expected because of the nature of (MB) dye. It is a substance that absorbs both UV and visible light and it simply reduces the extent of the radiation needed for the reaction of generating electron-hole pairs to initialize. Also, considering the fact that photocatalysis means adsorption of hydroxyl groups onto the photocatalyst surface and consequent hydroxyl radical formation, the abundance of MB molecules and their adsorption lowers the number of adsorption active sites and therefore decreases the rate of the reaction [62].

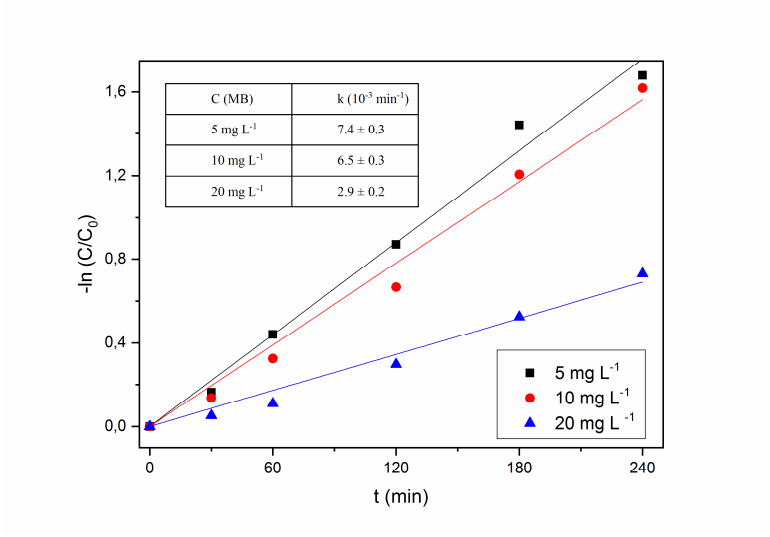

Figure 11. -ln(C/C_0) *vs.* time plot for photodegradation of MB with different concentrations from 5–20 mg L^{-1} under direct natural sunlight irradiation

3.7.4 Effect of medium pH

The pH value of the medium in which photocatalytic degradation takes place is also one of the crucial factors affecting the photocatalytic degradation of pollutants. The pH value determines the ionization state of the semiconductor surface and can affect the agglomeration of the photocatalyst material. In low pH electronic holes are the predominant oxygen species, while hydroxyl radicals are predominant in high pH [63]. Degradation of MB aqueous solution at different pH values (2, 4, 7, 9, 10 and 11) was investigated for $Co_{0.1}Mg_{0.9}Fe_2O_4$ (50 mg, 10 mg L^{-1} MB) under visible light. Corresponding kinetic curves calculated using first-order kinetics are displayed in Figure 12 and extracted reaction rates are shown as an inset in Figure 12. While degradation is negligible in acidic conditions, with the increase of pH there is a noticeable increment in photocatalytic activity. Higher pH values lead to effective photocatalytic degradation. This phenomenon can be explained with the abundance of hydroxyl radicals that participate in the oxidation of organic pollutants causing a higher rate of the reaction [64].

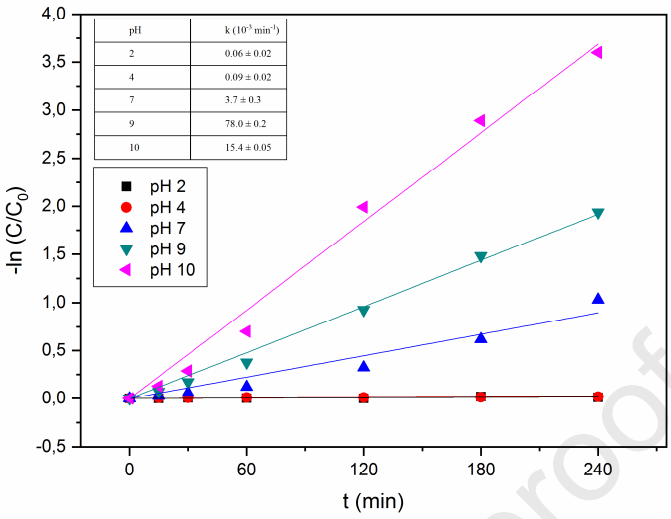

Figure 12. Influence of medium pH on degradation kinetics of methylene blue dye of $Co_{0.1}Mg_{0.9}Fe_2O_4$ (50 mg *vs.* 50 ml of 10 mg L^{-1} MB solution; visible light)

Conclusion

Mixed cobalt magnesium cubic spinel ferrites ($Co_xMg_{1-x}Fe_2O_4$ where $0 \leq x \leq 1$) were synthesized by a sol-gel combustion method. All synthesized powders consisted of multigrain agglomerates becoming more consolidated as the cobalt content increased. Structural analysis by X-ray diffraction, FTIR and Raman spectroscopy confirmed the formation of a partially inverse or inverse cubic spinel structure. The direct band gap of the materials decreased with an increase in the cobalt content (from 2.09 to 1.42 eV). Magnetization and coercivity increased with the cobalt content, which is the consequence of introducing additional unpaired electrons and stronger spin-orbit coupling of cobalt ions. The magnetic nature of the synthesized material is advantageous as the photocatalytic material can be efficiently removed. Photocatalytic measurements showed that photocatalytic efficiency did not differ substantially under natural sunlight or using an artificial visible light source, therefore solar energy could be used as a cheap energy source for water cleansing in a photocatalytic system. $Co_{0.1}Mg_{0.9}Fe_2O_4$ with the smallest mole percentage of cobalt showed the highest photocatalytic activity under visible light (79% of degradation after 4 hours of illumination). The optimum catalyst loading was determined

as 30 mg L^{-1}, for low concentrations of the pollutant (5 mg L^{-1}) aided by the increase of medium pH (10). Co-Mg ferrite systems could be further explored and optimized for the degradation of other pollutants.

Conflict of interest

The authors declare that they have no conflict of interest.

Acknowledgement

M. V. N., M. P. D., Z. Z. V., V. P. P. and N. B. T. acknowledge the support of the Ministry for Education, Science and Technological Development of the Republic of Serbia with contracts for realization and financing scientific research with the Institute for Multidisciplinary Research, University od Belgrade, no 451-03-68/202-14/200053 (Z. Z. V., M. V. N. and M. P. D.). D. B. and D. P. acknowledge the support of the project CeNIKS co-financed by the Croatian Government and the European Union through the European Regional Development Fund - Competitiveness and Cohesion Operational Programme (Grant KK.01.1.1.02.0013).

References

1. A. C. Druc, A. I. Borhan, A. Diaconu, A. R. Iordan, G. G. Nedelcu, L. Leonite, M. N. Palamaru, How cobalt ions substitution changes the structure and dielectric properties of magnesium ferrite?, Ceram. Int. 40 (2014) 13573-13578, https://doi.org/10.1016/j.ceramint.2014.05.071.
2. K. Kirchberg, A. Becker, A. Bloesser, T. Weller, J. Timm, C. Suchomski, R. Marschall, Stabilization of monodisperse, phase-pure $MgFe_2O_4$ nanoparticles in aqueous and nonaqueous media and their photocatalytic behaviour, J. Phys. Chem. C 121 (2017) 27126-27138, https://doi.org/10.1021/acs.jpcc.7b08780.
3. S. K. Durrani, S. Naz, M. Mehmood, M. Nadeem, M. Siddique, Structural, impedance and Mossbauer studies of magnesium ferrite synthesized via sol-gel auto-combustion process, J. Saudi Chem. Soc. 21 (2017) 899-910, https://doi.org/10.1016/j.jscs.2015.12.006.
4. K. Kombiah, J. Judith Vijaya, L. John Kennedy, K. Kaviyarasu, Catalytic studies of $NiFe_2O_4$ nanoparticles prepared by conventional and microwave combustion method,

Mater. Chem. Phys. 221 (2019), 11-28 https://doi.org/10.1016/j.matchemphys.2018.09.012

5. C. Barcena, A. K. Sra, G. S. Chaubey, C. Khemtong, J. P. Liu, J. Gao, Zinc ferrite nanoparticles as MRI contrast agents, Chem. Commun. (2008) 2224-2226, https://doi.org/10.1039/B801041B.
6. H. Habib, C. L. Ondeck, P. Chaudhary, M. R. Bockstaller, M. E. McHenry, Evaluation of iron-cobalt/ferrite core-shell nanoparticles for cancer thermotherapy, J. Appl. Phys. 103 (2008) 07A307, https://doi.org/10.1063/1.2830975.
7. K. Kombaiah, J. J. Vijaya, L. J. Kennedy, M. Bououdina, B. Al Najar, Self heating efficiency of $CoFe_2O_4$ nanoparticles: A comparative investigation on the conventional and microwave combustion method, J. Alloys Compd. 735 (2018) 1536-1545, https://doi.org/10.1016/j.jallcom.2017.11.279.
8. K. Kombaiah, J. J. Vijaya, L. J. Kennedy, M. Bououdina, B. Al-Najar, Conventional and microwave combustion synthesis of optomagnetic $CuFe_2O_4$ nanoparticles for hyperthermia studies, J. Phys. Chem. Solids 115 (2018) 162-171, https://doi.org/10.1016/j.jpcs.2017.12.024.
9. D. H. K. Reddy, Y.-S. Sun, Spinel ferrite magnetic adsorbents: Alternative future materials for water purification?, Coordin. Chem. Rev. 315 (2016) 90-111, https://doi.org/10.1016/j.ccr.2016.01.012.
10. K. Kefeni, B. B. Mamba, Photocatalytic application of spinel ferrite nanoparticles and nanocomposites in wastewater treatment: Review, SM&T 23 (2020) e00140 https://doi.org/10.1016/j.susmat.2019.e00140
11. T. Tatarchuk, M. Myslin, I. Mironyuk, M. Bououdina, A. T. Pedziwatr, R. Grgula, B. F. Bogacz, P. Kurzydio, Synthesis, morphology, crystallite size and adsorption properties of nanostructured Mg-Zn ferrites with enhanced porous structure, J. Alloys Compd. 819 (2020) 152945 https://doi.org/10.1016/j.jallcom.2019.152945
12. C. M. B. Henderson, J. M. Charnok, D. A. Plant, Cation occupancies in Mg, Co, Ni, Zn, Al ferrite spinels: a multi-element EXAFS study, J. Phys.: Condens. Matter. 19 (2007) 076214, https://doi.org/10.1088/0953-8984/19/7/076214.

13. D. S. Mathew, J.-S. Ruang, An overview of the structure and magnetism of spinel ferrite nanoparticles and their synthesis in microemulsions, Chem. Eng. J. 129 (2007) 51-65, https://doi.org/10.1016/j.cej.2006.11.001.
14. N. Thomas, V. D. Sudheesh, V. Sebastian, Magnetic and dieletric properties of magnesium substitued cobalt ferrite samples synthesized via one step calcination free solution combustion method, Ceram. Int. 43 (2017) 7305-7310, https://doi.org/10.1016/j.ceramint.2017.03.031.
15. A. Manikandan, M. Durka, S. A. Antony, Role of Mn^{2+} doping on structural, morphological and opto-magnetic properties of spinel $Mn_xCo_{1-x}Fe_2O_4$ (x=0, 0.1, 0.2, 0.3, 0.4, 0.5) nanocatalysts, J. Supercond. Nov. Magn. 28 (2015) 2047-2058, https://doi.org/10.1007/s10948-015-2987-8.
16. K. Kombiah, J. J. Viyaja, L. J. Kennedy, M. Bououdina, R. J. Ramalingam, H. A. Al Lohedan, Comparative investigation on the structural, morphological, optical and magnetic properties of $CoFe_2O_4$ nanoparticles, Ceram. Int. 43 (2017) 7682-7689 https://doi.org/10.1016/j.ceramint.2017.03.069
17. B. Jansi Rani, M. Ravina, B. Saravanakumar, G. Ravi, V. Ganesh, S. Ravichandran, Ferrimagnetism in cobalt ferrite ($CoFe_2O_4$) nanoparticles, Nano-Structures and Nano-Objects 14 (2018) 84-91, https://doi.org/10.1016/j.nanoso.2018.01.012.
18. D. Peddis, N. Yaacoub, M. Ferretti, A. Martinelli, G. Piccaluga, A. Musinu, C. Cannas, G. Navarra, J. M. Greneche, D. Fiorani, Cationic distribution and spin canting in $CoFe_2O_4$ nanoparticles, J. Phys.: Condens. Matter 23 (2011) 426004, https://doi.org/10.1088/0953-8984/23/42/426004.
19. J. Sharma, N. Sharma, J. Parashar, V. K. Saxena, D. Bhatnagar, Dielectric properties of nanocrystalline Co-Mg ferrites, J. Alloys Compd. 649 (2015) 362-367, https://doi.org/10.1016/j.jallcom.2015.07.103.
20. A. Godlyn Abraham, A. Manikandan, E. Manikandan, S. Vadivel, S. K. Jaganathan, A. Baykal, P. Sri Reganathan., Enhanced magneto-optical and photocatalytic properties of transition metal cobalt (Co^{2+} ions) doped spinel $MgFe_2O_4$ ferrite nanocomposites, J. Magn. Magn. Mater. 452 (2018) 38-388, https://doi.org/10.1016/j.jmmm.2018.01.001.

21. P. Chirawatkul, S. Khoonsap, S. Phumying, C. Kaewhan, S. Pinitsoontorn, S. Maensiri, Cation distribution and magnetic properties of $Co_xMg_{1-x}Fe_2O_4$ nanoparticles, J. Alloys Compnd 697 (2017) 249-256, https://doi.org/10.1016/j.jallcom.2016.12.106.
22. S. Marković, A. Stanković, J. Dostanić, Lj. Veselinović, L. Mančić, S. D. Škapin, G. Dražič, I. Janković-Častvan and D. Uskoković, Simultaneous enhancement of natural sunlight- and artificial UV-driven photocatalytic activity of a mechanically activated ZnO/SnO_2 composite, RSC Adv., (2017), **7**, 42725-42737, https://doi.org/10.1039/C7RA06895F.
23. D. K. Manimegalai, A. Mandikandan, S. Moortheswaran, S. A. Antony, Magneto-optical and photocatalytic properties of magnetically recyclable $Mn_xZn_{1-x}S$ (x = 0.0, 0.3 and 0.5) nanocatalysts, J. Supercond. Nov. Magn. 28 (2015) 2755-2766 https://doi.org/10.1007/s10948-015-3089-3
24. E. Casbeer, V. K. Sharma, X. Z. Li, Synthesis and photocatalytic activity of ferrites under visible light: A review, Sep. Purif. Tech. 87 (2012) 1-14, https://doi.org/10.1016/j.seppur.2011.11.034.
25. M. Sundararajan, L. J. Kennedy, P. Nithya, J. J. Vijaya, M. Bououdina, Visible light driven photocatalytic degradation of rhodamine B using Mg doped cobalt ferrite spinel nanoparticles synthesized by microwave combustion method, J. Phys. Chem. Solids 108 (2017) 61-75, https://doi.org/10.1016/j.jpcs.2017.04.002.
26. A. Mandikandan, M. Durka, S. A. Antony, Magnetically reciclable spinel $Mn_xZn_{1-x}Fe_2O_4$ ($0.0 \leq x \leq 0.5$) nanophotocatalysts, Adv. Sci. Eng. Med. 7 (2015) 33-46 https://doi.org/10.1166/asem.2015.1654
27. R. C. C. Costa, M. De Fatima Fontes Lelis, L. C. A. Oliveira, J. D. Fabris, J. D. Ardisson, R. R. V. A. Rios, C. N. Silva, R. M. Lago, Remarkable effect of Co and Mn on the activity of $Fe_{3-x}M_xO_4$ promoted oxidation of organic contaminants in aquaeous medium with H_2O_2, Catal. Commun. 4 (2003) 525-529, https://doi.org/10.1016/j.catcom.2003.08.002.
28. M. A. Venezuela, P. Bosch, J. Jimenez-Becerrill, O. Quiroz, A. I. Paez, Preparation, Characterization and photocatalytic activity of ZnO, Fe_2O_3 and $ZnFe_2O_4$, J. Photochem. Photobiol. A 148 (2002) 177-182, https://doi.org/10.1016/S1010-6030(02)00040-0.

29. B. H. Toby, R. B. Von Dreele, GSAS II: The genesis of a modern open-source all purpose crystallography software package, J. Appl. Crystallogr. 46 (2013) 544-549, https://doi.org/10.1107/S0021889813003531.

30. T. Yu, Z. X. Shen, Y. Shi, J. Ding, Cation migration and magnetic ordering in spinel $CoFe_2O_4$: micro-Raman scattering study, J. Phys.: Condens. Matter 14 (2002) L613-L618, DOI: 10.1088/0953-8984/14/37/101.

31. A. Mandikandan, M. Durka, S. A. Antony, A novel synthesis, structural, morphological and opto-magnetic characterizations of magnetically separable spinel $Co_xMn_{1-x}Fe_2O_4$ ($0 \leq x \leq 1$) nanocatalysts, J. Supercond. Nov. Magn. 27 (2014) 2841-2857 https://doi.org/10.1007/s10948-014-2771-1

32. L. Sun, R. Zhang, Q. Ni, E. Cao, W. Hao, Y. Zhang, Z. Ju, Magnetic and dielectric properties of $Mg_xCo_{1-x}Fe_2O_4$ ferrites prepared by the sol-gel method, Physica B 545 (2018) 4-11, https://doi.org/10.1016/j.physb.2018.05.030.

33. M. Gateshki, V. Petkov, S. K. Pradhan, T. Vogt, Structure of nanocrystalline $MgFe_2O_4$ from X-ray diffraction Rietveld and atomic pair distribution analysis, J. Appl. Cryst. 38 (2005) 772-779, https://doi.org/10.1107/S0021889805024477.

34. J. Venturini, A. M. Tonelli, T. B. Wermuth, R. Y. S. Zampiva, S. Arcaro, A. Da Cas Viegas, C. P. Bergmann, Excess of cations in the sol-gel synthesis of cobalt ferrite ($CoFe_2O_4$): A pathway to switching the inversion degree of spinels, J. Magn. Magn. Mater. 482 (2019) 1-8, https://doi.org/10.1016/j.jmmm.2019.03.057 .

35. P. Chandramohan, M. P. Srinivasan, S. Velmurgan, S. V. Narasimhan, Cation distribution and particle size effect on Raman spectrum of $CoFe_2O_4$, J. Solid State Chem. 184 (2011) 89-96, https://doi.org/10.1016/j.jssc.2010.10.019.

36. C. Murugesan, G. Chandravasetaran, Impact of Gd^{3+} substitution on structural, magnetic and electrical properties of cobalt ferrite nanoparticles, RSC Advances 5 (2015) 73714-73725, https://doi.org/10.1039/C5RA14351A.

37. M. Tsvetkov, M. Milanova, I. Ivanova, D. Neov, Z. Cherkezova-Zheleva, J. Zaharieva, M. Abrashev, Phase composition and crystal structure determination of cobalt ferrite modified with Ce, Nd and Dy ions by X-ray and neutron diffraction, J. Mol. Struct. 1179 (2019) 233-241, https://doi.org/10.1016/j.molstruc.2018.07.083.

38. T. Wang, T. Zhu, M. Brunet, C. Deshayes, P. Scian, Raman study of Yuan Qinghua porcelain: the highlighting of dendritic $CoFe_2O_4$ crystals in blue decorations, J. Raman Spectr. 48 (2017) 269-270, https://doi.org/10.1002/jrs.5029.
39. V. S. Puli, S. Adireddy, C. V. Ramana, Chemical bonding and magnetic properties of gadolinium (Gd) substituted cobalt ferrite, J. Alloys Compnd. 644 (2015) 470-475, https://doi.org/10.1016/j.jallcom.2015.05.031.
40. M. De, G. Bera, H. S. Tewary, Structural characterization of magnesium substituted nickel ferrite nanoparticles, Emerging Mater. Res. 6 (2017) 265-269 http://doi.org/10.1680/jemmr.1500070
41. R. S. Yadav, I. Kuritka, J. Vilcakova, J. Havlica, J. Masilko, L. Kalina, J. Tkacz, V. Enev, M. Hajdúchová, Structural, magnetic, dielectric, and electrical properties of $NiFe_2O_4$ spinel ferrite nanoparticles prepared by honey-mediated sol-gel combustion, J. Phys. Chem. Solids 107 (2017) 150-161, https://doi.org/10.1016/j.jpcs.2017.04.004.
42. Z. Z. Lazarevic, A. Milutinovic, D. Sekulic, V. N. Ivanovski, A. Recnik, B. Cekic, N. Z. Romcevic, Nanodimensional spinel $NiFe_2O_4$ and $ZnFe_2O_4$ ferrites prepared by soft mechanochemical synthesis, J. Appl. Phys. 113 (2013) 187221, https://doi.org/10.1063/1.4801962.
43. J. P. Singh, R. C. Srivastava, H. M. Agrawal, R. Kumar, Micro-Raman investigation of nanosized zinc ferrite: effect of crystallite size and fluence of irradiation, J. Raman Spectr. 42 (2011) 1510-1517, https://doi.org/10.1002/jrs.2902.
44. K. S. A. Kumar, R. Bhowmik, Micro-structural characterization and magnetic study of $Ni_{1.5}Fe_{1.5}O_4$ ferrite synthesized through coprecipitation route at different pH values, Mater. Chem. Phys. 146 (2014) 159-169, https://doi.org/10.1016/j.matchemphys.2014.03.015.
45. S. G. Gawas, S. S. Meena, P. Bhatt, V. M. S. Verenkar, Nanoscale-driven structural changes and associated superparamagnetism in magnetically diluted Ni-Zn ferrites. Mater. Chem. Front., 2 (2018) 300-312, https://doi.org/10.1039/C7QM00437K.
46. S. W. da Silva, F. Nakagomi, M. S. Silva, A. Franco Jr, V. K. Garg, A. C. Oliveira, P. C. Morais, Raman study of cations' distribution in $Zn_xMg_{1-x}Fe_2O_4$ nanoparticles. J. Nanopart. Res. 42 (2012) 1-10, https://doi.org/10.1007/s11051-012-0798-4.

47. Z. Yan, J. Gao, Y. Li, M. Zhang, M. Guo, Hydrothermal synthesis and structure evolution of metal-doped magnesium ferrite from saprolite laterite, RSC Advances, 5 (2015) 927778-992787, https://doi.org/10.1039/C5RA17145H.

48. B. Nandan, M. C. Bhatnagar, S. C. Kashyap, Cation distribution in nanocrystalline cobalt substituted nickel ferrites: X-ray diffraction and Raman spectroscopic investigations, J. Phys. Chem. Solids 129 (2019) 298-306, https://doi.org/10.1016/j.jpcs.2019.01.017.

49. P. N. Anantharamaiah, P. A. Joy, Enhancing the strain sensitivity of $CoFe_2O_4$ at low magnetic fields without affecting the magnetostriction coefficient by substitution of small amounts of Mg for Fe, Phys. Chem. Chem. Phys. 15 (2016) 10516-10527, https://doi.org/10.1039/C6CP00369A.

50. H. S. Mund, B. L. Ahuja, Structural and magnetic properties of Mg doped cobalt ferrite nanoparticles prepared by sol-gel method, Mater. Res. Bull. 85 (2017) 228-233, https://doi.org/10.1016/j.materresbull.2016.09.027.

51. C. O. Ehi-Erimosele, E. E. J. Iweala, Low-temperature combustion synthesis of cobalt magnesium ferrite magnetic nanoparticles: effects of fuel-to-oxidizer ratio and sintering temperature, J. Sol-Gel Sci. Technol. 76 (2015) 298-308, https://doi.org/10.1007/s10971-015-3777-2.

52. H. Assi, S. Atiq, S. M. Rammay, N. S. Alzayed, M. Saleem, S. Riaz, S. Naseem, Substituted Mg-Co ferrite: recyclable magnetic photocatalyst for the reduction of methylene blue and degradation of toxic dyes, J. Mater. Sci.: Mater. Electron. 28 (2017) 2250-2256, https://doi.org/10.1007/s10854-016-5795-4.

53. J. Tauc, A. Menth, D. L. Wood, Optical and magnetic investigations of the localized states in semiconducting glasses, Phys. Rev. Lett. 25 (1970) 2378-2385, https://doi.org/10.1103/PhysRevLett.25.749

54. M. H. Habibi, H. J. Parhizkar, FTIR and UV-vis diffuse reflectance spectroscopy studies of the wet chemical (WC) route synthesized nano-structure $CoFe_2O_4$ from $CoCl_2$ and $FeCl_3$, Spectrochim. Acta A, 127 (2014) 102-106, https://doi.org/10.1016/j.saa.2014.02.090.

55. A. Mandikandan, R. Sridhar, A. A. Antony, S. Ramakrishna, A simple aloe vera plant extracted microwave and conventional combustion synthesis: Morphological, optical,

magnetic and catalytic properties of $CoFe_2O_4$ nanostructures, J. Mol. Struct. 1076 (2014) 188-200 https://doi.org/10.1016/j.molstruct.2014.07.054

56. A. Goldman: Modern ferrite technology, 2nd ed. NY, Springer (2010), https://doi.org/10.1007/978-0-387-29413-1
57. L. Gan, S. Shang, C. W. M. Yuen, S. Jiang, E. Hu, Hydrothermal synthesis of magnetic CoFe2O4/graphene nanocomposites with improved photocatalytic activity, Applied Surface Science 351 (2015) 140-147, https://doi.org/10.1016/j.apsusc.2015.05.130
58. A. Sutka, G. Mezinskis, Sol-gel auto-combustion synthesis od spinel-type ferrite nanomaterials, Front. Mater. Sci. 6 (2012) 128-141, https://doi.org/10.1007/s11706-012-0167-3.
59. I. J. C. Lynda, M. Durka, A. Dinesh, A. Manikandan, S. K. Jaganthan, A. Baykal, S. A. Antony, Enhanced Magneto-optical and Photocatalytic Properties of Ferromagnetic Mg 1-y Niy Fe2O4 (0.0<y<1.0) Spinel Nano-ferrites, J. Supercond. Nov. Magn., 31 (2018) 3637-3647 https://doi.org.10.1007/s10948-018-4623-x
60. G. Padmapriya, A. Manikandan, V. Krishnasamy, S. K. Jaganathan, S. Arul Anton, Spinel NixZn1-xFe24 (0.0<x<1.0) nano photo-catalysts: Synthesis, characterization and photocatalytic degradation of methylene blue, J. Mol. Struct. 1119 (2016) 39-47 https://doi.org/10.1016/j.molstruc.2016.04.049
61. A. Nageswara Rao, B. Sivasankar, V. Sadasivam, Kinetic studies on the photocatalytic degradation of Direct Yellow 12 in the presence of ZnO catalyst, J. Mol. Catal. A - Chem. 306 (2009), 77-81, https://doi.org/10.1016/j.molcata.2009.02.028
62. R. Farouq, Investigation of the kinetics and optimization of photocatalytic degradation of methylene blue, J. Chi. Chem. Soc. (2018) 1-7, https://doi.org/10.1002/jccs.201800029.
63. U.G. Akpan, B.H. Hameed, Parameters affecting the photocatalytic degradation of dyes using TiO2-based photocatalysts: A review, J. Hazard. Mater. 170 92009) 520-529 https://doi.org/10.1016/j.jhazmat.2009.05.039
64. W. Chu, W. K. Choy, T. Y. So, Effect of solution pH in the TiO_2 -induces photocatalysis of chlorinated aniline, J. Hazard. Mat. 141 (2007) 86-91, https://doi.org/10.1016/j.jhazmat.2006.06.093.

Highlights

- Sol-gel synthesis of nano semiconductors is simple, low-cost and efficient
- Mg-Co ferrite spinels can be used as catalysts in photocatalytic water purification
- Efficency depends on particle size, band gap, agglomeration, pH, catalyst loading

Declaration of interests

☒ The authors declare that they have no known competing financial interests or personal relationships that could have appeared to influence the work reported in this paper.

☐The authors declare the following financial interests/personal relationships which may be considered as potential competing interests: